Dalton Transactions

ROYAL SOCIETY OF CHEMISTRY

PAPER

View Article Online
View Journal | View Issue

Cite this: *Dalton Trans.*, 2025, **54**, 4039

Three-dimensional hollow ZnS/MXene heterostructures with stable Ti–O–Zn bonding for enhanced lithium-ion storage†

Wei Yang,[a] Wenqing Wang,[a] Shidi Huang,*[b] Mengluan Gao,[a] Fuming Weng[a] and Rujia Zou *[a]

An effective way to improve the cycling performance of metal sulfide materials is to blend them with conductive materials. In this paper, three-dimensional (3D) hollow MXene/ZnS heterostructures (ZnSMX) were prepared *via* a two-step process involving hydrothermal and template methodologies. The formation of Ti–O–Zn bonds enables the firm bonding between ZnS nanoparticles and the MXene substrate at heterogeneous interfaces, which can act as "electron bridges" to facilitate electron and charge transfer. Additionally, 3D hollow ZnSMX not only enhances the conductivity of ZnS, enabling rapid charge transfer, but also effectively show restacking of MXene nanosheets to maintain structural stability during the charge/discharge process. More importantly, the 3D porous structure provides ultrafast interfacial ion transport pathways and extra surficial and interfacial storage sites, thus boosting excellent storage performances in lithium-ion battery applications. The 3D ZnSMX exhibited a high capacity of 782.1 mA h g^{-1} at 1 A g^{-1} current, excellent cycling stability (providing a high capacity of 1027.8 mA h g^{-1} after 350 cycles at 2 A g^{-1}), and excellent rate performance. This indicates that 3D ZnS/MXene heterostructures can potentially be highly promising anode materials for high-multiplication lithium-ion batteries.

Received 5th December 2024,
Accepted 27th January 2025

DOI: 10.1039/d4dt03381g

rsc.li/dalton

1. Introduction

Lithium-ion batteries (LIBs) have become the principal energy source for portable electronic devices and electric vehicles due to their high energy density and number of cycles.[1] Nevertheless, the graphite anode, which is currently the most commonly used, has a low theoretical capacity (372 mA h g^{-1}) and unsatisfactory rate performance.[2–4] Consequently, it is of great importance to explore alternative anode materials with a large capacity and fast reaction kinetics to improve the energy/power density of LIBs. Transition metal sulfides (TMSs), including MoS_2, SnS, CoS, and ZnS, have emerged as a promising class of advanced anode-active materials for LIBs due to their high specific capacity and rich interfacial redox chemistry.[5–8] Among these materials, ZnS with a high specific capacity (962 mA h g^{-1}) and low cost is regarded as an optimal electrode material for energy storage.[9] However, pure ZnS materials show poor rate and cycling performance due to their poor electrical conductivity and large volume changes during cycling.[10]

In order to overcome these shortcomings, designing an architecture of particles at the nanoscale combined with highly conductive materials has been proposed. Nanostructuring facilitates the formation of a high surface area, which improves the feasibility of electrolyte wetting and reduces the migration path for Li-ion transportation. Furthermore, reducing the particle size reduces the physical strain that occurs during electrochemical lithiation/delithiation.[11,12] For example, Zhai *et al.* reported a p-ZnS@CN composite featuring a 3D interconnected hierarchical pore structure, and the as-prepared p-ZnS@CN sample showed 533.6 mA h g^{-1} at 1 A g^{-1} over 200 cycles.[13] While the introduction of carbon decoration can enhance the electrochemical performance to a certain degree, the inherent physical binding of TMS to adjacent carbon atoms results in inefficient contact, leading to unintentional disconnection and retarded charge transfer kinetics.[14] MXenes, a new class of two-dimensional (2D) materials, have garnered significant interest due to their excellent conductivity and large specific surface area.[15] Among them, $Ti_3C_2T_x$ MXenes have attracted considerable attention due to their high lithium diffusion mobility, abundance of surface functional groups, and hydrophilicity.[16] Therefore, the utilization of MXenes as an efficacious conductive substrate can prove highly effective in enhancing active materials such

[a]*State Key Laboratory of Advanced Fiber Materials, College of Materials Science and Engineering, Donghua University, Shanghai 201620, China. E-mail: rjzou@dhu.edu.cn*
[b]*School of Ecological Technology and Engineering, Shanghai Institute of Technology, Shanghai 201418, P. R. China. E-mail: sdhuang@sit.edu.cn*

† Electronic supplementary information (ESI) available. See DOI: https://doi.org/10.1039/d4dt03381g

as TMSs and other active materials with low intrinsic conductivity (such as SnO_2, Co_3O_4, and Si).[17–21] However, as is the case with other 2D materials such as graphene, the MXene nanosheets inside active materials are prone to forming irreversible agglomerations *via* van der Waals forces, which can hinder ion transport, reduce the utilization of reaction sites, and increase ion/electron transport distances, leading to poor rate and cycling performance.[22–25] A common strategy to address this shortcoming is to prepare MXene nanosheets into three-dimensional (3D) structures. Yao *et al.* reported a 3D porous MXene aerogel threaded hollow CoS nanobox composite with excellent electron and ion transport properties which shows excellent cycling stability and high capacities.[26] While the construction of 3D structured MXenes holds considerable promise for the design of negative electrode materials, to our knowledge, no report exists on the preparation of 3D structured composites of ZnS and MXenes.

In this study, zinc sulfide (ZnS) nanoparticles were grown *in situ* on MXene nanosheets to form 3D hollow ZnSMX using a hydrothermal method, followed by a template method. The incorporation of ZnS nanoparticles into 3D ZnSMX enables the reduction of lithium diffusion distances in the solid phase, thereby enhancing the electrochemical kinetic performance. In addition, the effective enhancement of conductivity by MXenes in the heterostructures facilitates rapid electron transfer while simultaneously preventing the aggregation of ZnS nanoparticles. More importantly, the ZnS nanoparticles can be firmly attached to the MXene nanosheets through the formation of interfacial Ti–O–Zn bonds, which effectively prevents the detachment of ZnS nanoparticles from the conducting MXene substrate and adapts to the volume changes of ZnS during the charge/discharge process. The 3D porous structure reduces the self-stacking of MXene nanosheets, thereby exposing a larger number of reactive sites and facilitating the rapid penetration of electrolytes. The 3D ZnSMX shows remarkable long-term cycling stability, retaining a capacity of 1027.8 mA h g^{-1} even after 350 cycles at 2 A g^{-1} and superior rate performance.

2. Experimental section

2.1 Synthesis of $Ti_3C_2T_x$ MXene nanosheets

$Ti_3C_2T_x$ MXene nanosheets were prepared using a typical etching method. Initially, 1.6 g LiF powder was placed into a Teflon beaker containing 20 milliliters of 9 M HCl, with stirring maintained throughout the process. 1.0 g Ti_3AlC_2 powder was added slowly after LiF was completely dissolved in the above solution. Then, the mixture was heated at 40 °C for 24 h under continuous stirring. Subsequently, the mixed solution was washed and centrifuged with deionized water (DI water) at a speed of 3500 rpm until the pH value of the supernatant was close to 6. The resulting multilayered $Ti_3C_2T_x$ MXene was mixed with 100 mL DI water and ultrasonicated for 1 h under an argon atmosphere. Finally, the MXene nanosheet suspension was obtained by centrifugation at 3500 rpm for 1 h. The concentration of MXene nanosheet suspension was measured at 4 mg mL^{-1} by freeze-drying.

2.2 Synthesis of ZnS/MXene heterostructures

In this procedure, 5 mL $Ti_3C_2T_x$ MXene suspension and 35 mL DI water were put into a Teflon liner (60 mL) followed by adding 75.3 mg zinc acetate. When the mixture was stirred for 1 h, 342 mg thioacetamide was added under continuous stirring. Following a 10-minute stirring period, the mixed solution was subjected to a hydrothermal reaction in a Teflon steel reaction vessel maintained at 60 °C for 4 hours. During this period, ZnS nanoparticles were grown on MXene nanosheets. The product was washed with DI water five times and dried by freeze-drying at −50 °C for 12 hours. The mass ratio of ZnS was calculated to be 67%. For purposes of comparison, pure ZnS was prepared using the same method, but without the addition of the MXene suspension.

2.3 Synthesis of polystyrene (PS) spheres

The PS spheres were initially prepared through dispersion polymerization of styrene with ammonium persulfate (APS) as the initiator. This process entailed the dissolution of 20 mg polyvinyl pyrrolidone and 20.5 mg APS in a mixture solution comprising 46 mL of ethanol and 6 mL of DI water. Subsequently, 4.4 mL of styrene monomer was added to the solution. The polymerization was conducted at 70 °C in an oil bath for 24 hours. Following this, the reactor was cooled in ice water for 30 minutes, after which the final PS spheres were collected by centrifuging and washing the white solution with DI water five times.

2.4 Synthesis of 3D ZnSMX heterostructures

A specific quantity of PS spheres was introduced into the ZnS/MXene heterostructure aqueous solution (with a mass ratio of PS to $Ti_3C_2T_x$ of 3 : 1) and subjected to sonication for 10 minutes in order to facilitate the formation of a uniform dispersion. Following the freeze-drying process, the resulting powder was collected and subsequently annealed at a temperature of 450 °C for a duration of 1 hour under the flow of argon, intending to remove the PS.

2.5 Material characterization

The morphology and structure of the as-prepared samples were characterized using scanning electron microscopy (SEM, Hitachi S-4800) and transmission electron microscopy (TEM, JEM-2100F). X-ray diffraction (XRD) patterns were collected by using a D/max-2550 PC XRD (Rigaku, CuKα radiation). X-ray photoelectron spectroscopy (XPS) spectra were obtained on an Escalab 250Xi. Nitrogen adsorption/desorption isotherms were obtained using the ASAP 2020 instrument and the specific area was calculated by the BET method.

2.6 Electrochemical measurements

The electrodes were prepared by mixing the active material, carbon black, and PVDF (mass ratio of 8 : 1 : 1) with *N*-methyl-2-pyrrolidone (NMP) to form an electrode slurry. The prepared

uniform slurry was evenly coated on Cu foil and subsequently subjected to vacuum drying at 60 °C for 12 h. Lithium foil and monolayer polypropylene film (Celgard 2500) were employed as the counter electrode and separator, respectively, and 1 M $LiPF_6$ in ethylene carbonate (EC)/diethyl carbonate (DEC) (1 : 1 by volume) was utilized as the electrolyte. The electrochemical performance of the CR-2032 coin-type cells was evaluated after assembling them in an argon-filled glove box (H_2O < 1 ppm, O_2 < 1 ppm). Galvanostatic charge–discharge tests were conducted on a LANDHE measurement system with a cut-off voltage range of 0.01–3.0 V. The estimated capacity was determined by measuring the mass of the ZnS/MXene hybrid. The electrochemical workstation (Metrohm Autolab) was employed to conduct CV measurements over the potential range of 0.01–3.0 V and electrochemical impedance spectroscopy (EIS) in the frequency range of 0.01–100 kHz. The galvanostatic intermittent titration technique (GITT) test involved applying a current pulse of 0.1 A g^{-1} for 20 minutes, followed by a relaxation phase of 1 hour, utilizing the LANDHE measurement system.

3 Results and discussion

The synthesis of the 3D ZnS/MXene heterostructures (ZnSMX) is shown schematically in Fig. 1. The typical mild method was employed to prepare the MXene nanosheets.[27] Ti_3AlC_2 powder was etched with LiF and HCl, and then the wet precipitates obtained by centrifugation were sonicated in order to obtain monolayer $Ti_3C_2T_x$ MXene nanosheets. The surface of 2D MXene nanosheets is negatively charged due to the presence of functional groups such as –OH, –O, and –F.[28] Positively charged Zn^{2+} are electrostatically adsorbed onto the surface of the MXene nanosheets, facilitating the *in situ* growth of ZnS particles on MXene nanosheets to form the ZnS/MXene nanosheet composite by hydrothermal reaction.[29] In the process of this reaction, the MXene nanosheets remained stable due to the low reaction temperature. In addition, the ZnSMX nanosheets exhibited excellent dispersion in DI water after simple sonication. Then, the ZnSMX dispersion was mixed with the PS dispersion for 15 minutes, followed by freeze-drying the mixture to obtain the PS/ZnSMX powder. Finally, the PS template was removed through thermal annealing at 450 °C under an argon atmosphere, thus obtaining the 3D ZnSMX.

The morphologies and structures of ZnSMX have been characterized by scanning electron microscopy (SEM) and transmission electron microscopy (TEM). As illustrated in Fig. 2a, the MXene nanosheets were uniformly loaded with ZnS nanoparticles, exhibiting nanoparticle sizes within the range of 20–30 nm. Fig. 1b and c present different magnification SEM images of 3D ZnSMX which reveal that the 3D spherical morphology of ZnSMX is well preserved after self-assembly with PS spheres and subsequent annealing treatment. As can be observed in Fig. 2c and Fig. S1a,† the diameter of the ZnSMX hollow spheres is approximately 800 nm. Fig. 2d and e show the TEM images of pure MXene nanosheets and ZnSMX after the hydrothermal reaction, respectively. A comparison of Fig. 2d and e illustrates that MXene nanosheets retain their monolayer structure even after undergoing the hydrothermal process. In addition, Fig. 2e further demonstrates that ZnS nanoparticles are uniformly grown on MXene nanosheets. The lattice spacing was determined to be 0.31 nm, which corresponds to the (111) lattice plane of cubic ZnS, as shown in Fig. 1f. The energy-dispersive spectroscopy (EDS) elemental mapping of ZnSMX shown in Fig. 2g–j displays the uniform distribution of Zn, Ti, and S elements throughout the samples, indicating that the rough surface of the MXene nanosheet is composed of a significant number of ZnS nanoparticles.

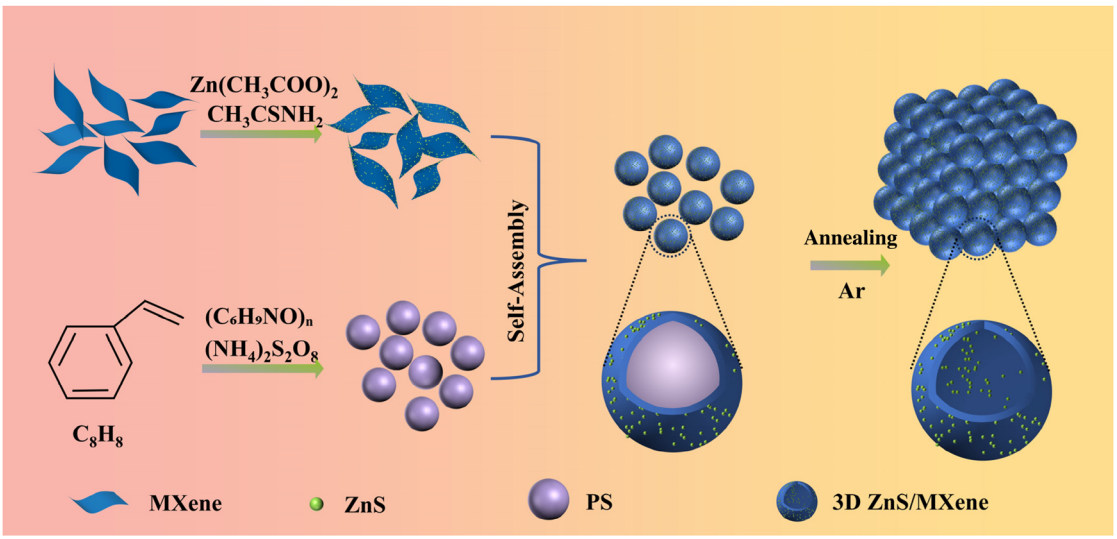

Fig. 1 Schematic diagram of the 3D ZnSMX synthetic route.

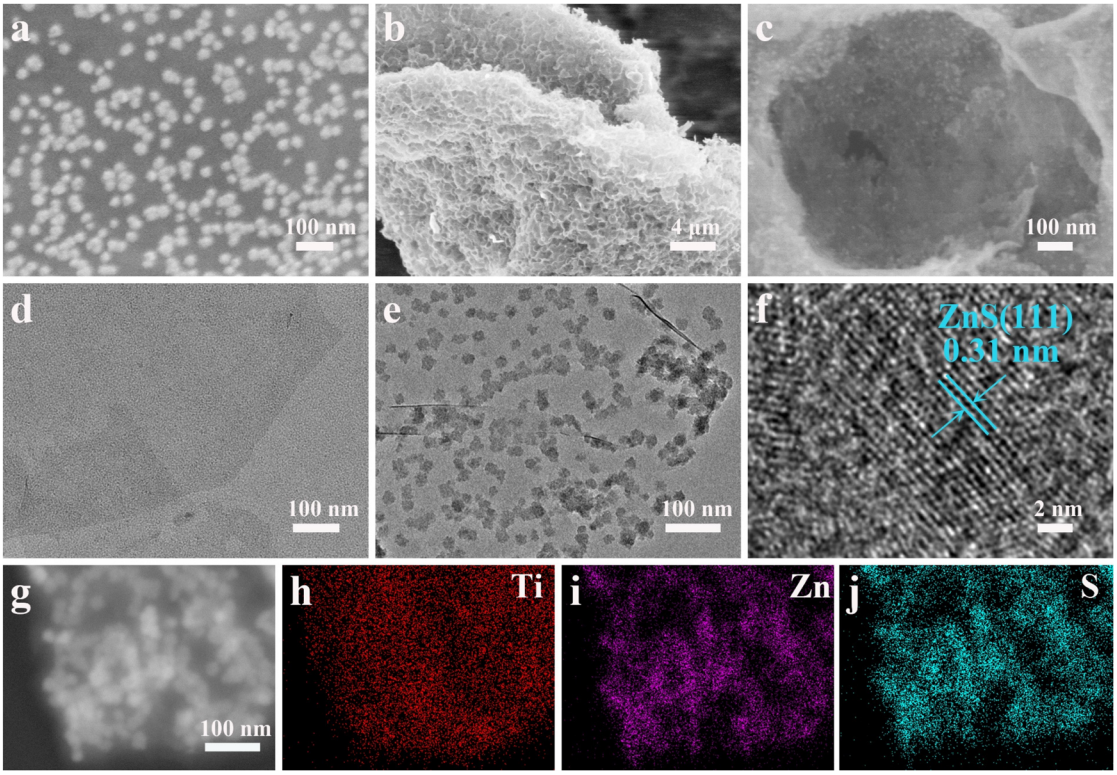

Fig. 2 (a) SEM images of ZnSMX. (b and c) Different magnification SEM images of 3D ZnSMX. (d) TEM images of MXene. (e) TEM images of ZnSMX. (f) HRTEM images of ZnSMX. (g–j) EDS elemental mapping images of Ti, Zn, and S elements in ZnSMX.

Fig. S2† shows the X-ray diffraction (XRD) patterns of Ti_3AlC_2 and $Ti_3C_2T_x$ MXene nanosheets. A comparison of the XRD patterns of Ti_3AlC_2 and MXene reveals the disappearance of the characteristic (104) peak at approximately 39.0° for Ti_3AlC_2, which indicates that the Al layer in Ti_3AlC_2 has been successfully removed by LiF/HCl etching.[30] Furthermore, the (002) peak of MXene moves to a lower angle after etching compared with that of Ti_3AlC_2, which provides further evidence of the successful synthesis of Ti_3C_2 MXene.[31] Fig. 3a shows the XRD patterns of ZnSMX, MXene, and ZnS. The ZnSMX prepared by the hydrothermal method shows characteristic peaks of MXene and ZnS. Three diffraction peaks are observed at 2θ of 28.9°, 48.5°, and 57.2°, which are seen as the (111), (220), and (311) planes of the cubic structure of ZnS while the peak at approximately 6.2° is identified as the characteristic (002) peak of MXene.[32] The above results indicate that ZnS nanoparticles have been successfully grown *in situ* on MXene nanosheets using the hydrothermal method.

X-ray photoelectron spectroscopy (XPS) was performed to probe the composition and electronic valence state of ZnSMX. The survey spectrum in Fig. S3a† proves the presence of Zn, S, C, Ti, and O elements in the ZnSMX sample. High-resolution XPS spectra of ZnS and MXene are shown in Fig. S3b–e.† Fig. 3b shows the binding energies at about 1044.4 eV and 1021.3 eV are attributed to Zn $2p_{1/2}$ and Zn $2p_{3/2}$ which proves the existence of Zn^{2+}.[33] Meanwhile, the binding energies of S 2p at around 162.6 eV ($2p_{1/2}$) and 161.4 eV ($2p_{3/2}$) in Fig. 3c are found to be consistent with those observed in ZnS.[33] The binding energies of C 1s are fitted by three peaks at 281.7 eV (C–Ti), 284.8 eV (C–C), and 286.2 eV (C–O). The C–Ti bond from $Ti_3C_2T_x$ MXene (281.7 eV) demonstrates that the MXene nanosheets remained intact and unoxidized during synthesis.[34] Fig. 3e illustrates the presence of multiple peaks of Ti 2p at around 454.9 eV (460.5 eV), 455.8 eV (461.4 eV), 456.7 eV (462.4 eV), and 458.5 eV (463.9 eV), which are attributed to Ti–C, Ti^{2+}, Ti^{3+}, and Ti–O bonds of $Ti_3C_2T_x$ MXene.[32] As illustrated in Fig. 3f, the high-resolution XPS spectra of O 1s was utilized to investigate the interfacial interaction state of MXene and ZnS. The binding energies of O 1s at 529.5 eV, 530.3 eV, 531.3 eV, and 533.1 eV are identified as O–Ti, C–Ti–O_x, Ti–O–Zn, and O–H bonds. The Ti–O–Zn bonds indicate that new chemical bonds are formed at the interface between ZnS and MXene, which derives from the *in situ* growth of ZnS on the MXene nanosheet substrate.[35] Here, the XPS results further demonstrate that the ZnS nanoparticles are securely attached to the MXene nanosheets, enabling stable generation within its interlayer spaces and improving the overall electrochemical kinetics of the material. As illustrated in Fig. S9,† the BET results indicate that the specific surface area of 3D ZnSMX nanorods is 111.14 $m^2\ g^{-1}$, whereas that of 2D ZnSMX is only 18.87 $m^2\ g^{-1}$. The pore volumes of 3D ZnSMX and 2D ZnSMX are around 0.202 $cm^3\ g^{-1}$ and 0.053 $cm^3\ g^{-1}$. This observation suggests that the 3D hollow spherical structure effectively hinders the reaccumulation of ZnSMX, thereby enhancing the specific

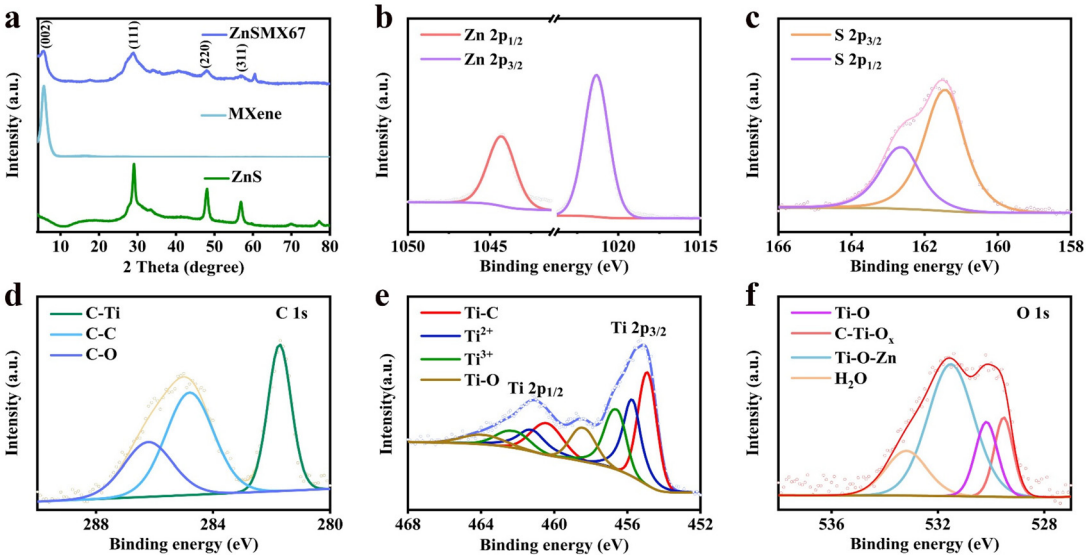

Fig. 3 (a) XRD patterns of ZnS, MXene, and ZnSMX. (b–f) High-resolution XPS spectra of Zn 2p, S 2p, C 1s, Ti 2p, and O 1s for ZnSMX.

surface area of MXene. The high porosity of 3D ZnSMX facilitates adaptation to volume expansion during cycling and accelerates ion transport.

The electrochemical properties of the 3D ZnSMX, ZnS, and MXene were evaluated by CV at a scanning rate of 0.2 mV s^{-1}, as shown in Fig. 4a, b, and Fig. S4.† The pronounced peaks observed between 1.0 and 0.4 V in the initial cathodic scan are attributed to the decomposition of the electrolyte and the formation of the solid electrolyte interphase (SEI). The cathodic peak at 1.65 V in the initial curve is identified as the conversion reaction between ZnS and Zn/Li_2S. During the anodic polarization, several small peaks are observed between 0.01 and 0.70 V, indicating that Li^+ is extracted from the formed Li–Zn alloys, signifying the multistep dealloying process of Li–Zn alloys. The similarity of the CV curves in the second and third cycles demonstrates the excellent cycle reversibility of the 3D ZnSMX electrode. In light of the findings presented in the CV result, it is proposed that the electrochemical reactions of cubic ZnS can be described as follows:

$$ZnS + 2Li^+ + 2e^- \rightleftharpoons Li_2S + Zn$$

$$Zn + xLi^+ + xe^- \rightleftharpoons Zn/Li_x$$

Fig. 4c and Fig. S5† illustrate the galvanostatic charge–discharge (GCD) profiles of 3D ZnSMX, 2D ZnSMX, ZnS, and MXene electrodes at 0.2 A g^{-1} for the initial three cycles, which align with the results of the CV tests mentioned above. The 3D ZnSMX electrode exhibits the most excellent first cycle discharge–charge capacity of 1784.6/1072.9 mA h g^{-1} with an initial coulombic efficiency (ICE) of 60.3%, which is obviously higher than those of 2D ZnSMX, ZnS, and MXene. The low CE values observed can be attributed to the formation of SEI membranes in the initial cycle which leads to a significant capacity loss. In subsequent cycles, however, the CE values approach 100%. This indicates that the resulting composite materials exhibit excellent reversibility during cycling. The comparative analysis of the cycling performance of 3D ZnSMX, 2D ZnSMX, ZnS, and MXene electrodes at 1 A g^{-1} is presented in Fig. 4d. It is evident that the pure ZnS electrode exhibits a rapid decline in capacity, reaching 187.5 mA h g^{-1} within twenty cycles. The rapid capacity decay can be attributed to the pulverization of ZnS, which is a consequence of the considerable volume change that occurs during the charge/discharge process. Obviously, the 3D ZnSMX electrode exhibits a higher reversible capacity than 2D ZnSMX which is attributed to the interconnected conductive network structure facilitating fast electron/ion transport and exposing more ZnS nanoparticles. In addition, the rate performance of 3D ZnSMX, 2D ZnSMX, ZnS and MXene electrodes was evaluated at various current densities from 0.2 to 5.0 A g^{-1}, as shown in Fig. 4e. The 3D ZnSMX electrode shows high specific capacities at current densities of 0.2, 0.5, 1.0, 2.0, and 5.0 A g^{-1} as 961.6, 857.4, 782.1, 693.3, and 598.1 mA h g^{-1} respectively. In comparison with 3D ZnSMX, the capacities for pure ZnS electrode only reached 317.4, 219.6, 154.5, 97.6, and 38.9 mA h g^{-1} at current densities of 0.2, 0.5, 1.0, 2.0, and 5.0 A g^{-1}, respectively. During the charge/discharge process, the pure ZnS nanoparticles suffered from agglomeration problems which caused sluggish lithium-ion storage kinetics leading to unsatisfactory rate performance. There is no doubt that 3D ZnSMX electrode demonstrates excellent rate performance compared to other samples of 2D ZnSMX, ZnS, and MXene electrodes in this research. In particular, compared to previously reported ZnS-based composite electrodes shown in Fig. 4f, the 3D ZnSMX electrode exhibits better rate performance at both low and high current densities.[36–45] Based on the excellent rate performance of the 3D ZnSMX, the long-term cycling behavior of 3D ZnSMX at 2.0

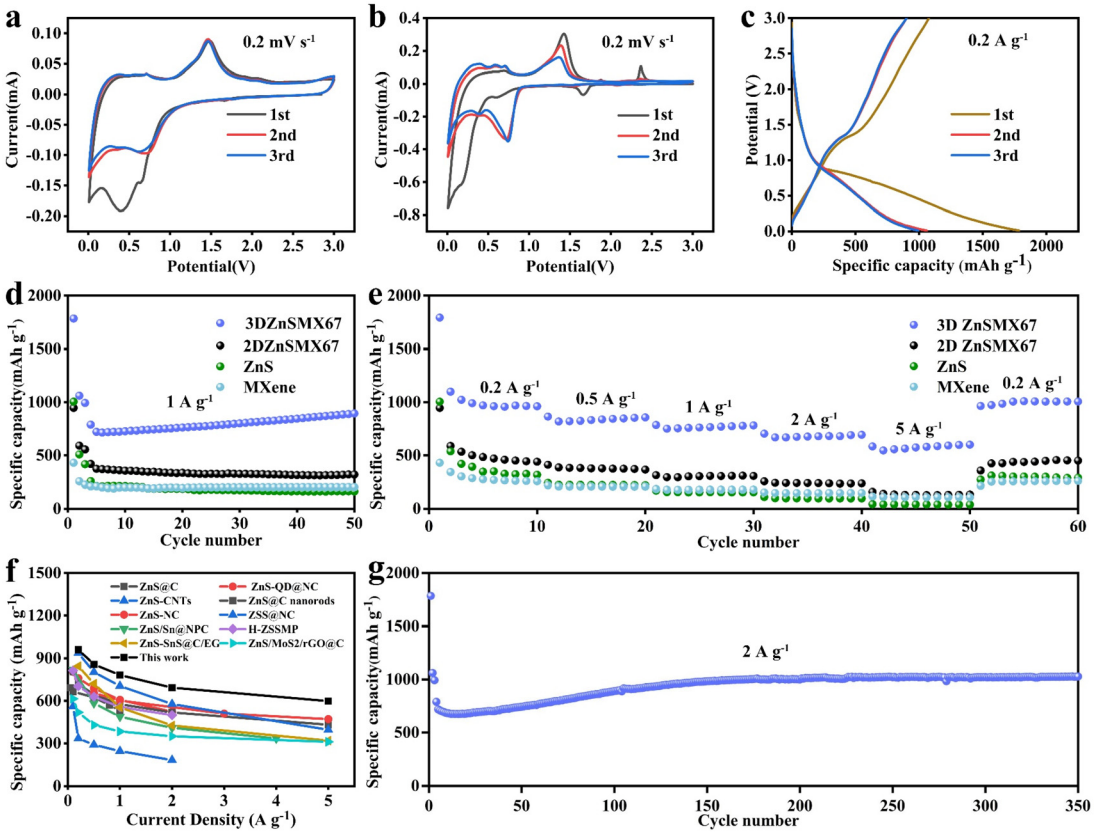

Fig. 4 (a) CV curves of the 3D ZnSMX electrode at 0.2 mV s^{-1} for the first three cycles. (b) CV curves of the ZnS electrode at 0.2 mV s^{-1} for the first three cycles. (c) GCD profiles of the 3D ZnSMX electrode at 0.2 A g^{-1} for the initial three cycles. (d) Cycling stability and (e) rate performance of the 3D ZnSMX, 2D ZnSMX, ZnS, and MXene electrodes. (f) Comparison of the rate performance of the 3D ZnSMX electrode with reported ZnS-based composite anodes. (g) Long-term cycling performance of 3D ZnSMX electrode at 2 A g^{-1}.

A g^{-1} and 5.0 A g^{-1} was also investigated, as illustrated in Fig. 4g and Fig. S7.† Following 350 cycles at current densities of 2.0 A g^{-1}, the specific capacity of 3D ZnSMX electrodes reached 1027.8 mA h g^{-1}, a value that exceeds the performance of previously reported ZnS-based electrodes.[36–45] The specific capacity of the 3D ZnSMX electrode was found to remain at 493.9 mA h g^{-1} even after 800 cycles at 5.0 A g^{-1}. It is noteworthy that the capacity of the 3D ZnSMX electrode exhibits an evident increasing trend during battery cycling, a phenomenon commonly observed in the anodes of most TMSs and TMOs.[46,47] By comparing the GCD curves of the 10th, 50th, 100th, 150th, and 200th cycles shown in Fig. S8a,† it is evident that the increase in capacity primarily occurs in the low-volt interval (0.01–0.50 V), which may be due to the reversible formation and decomposition of the gel-like polymer layer in the electrolyte.[48] The gel-like polymer layer that forms at the interface between the electrode and the electrolyte has the potential to generate an excess of interfacial storage through pseudocapacitive behavior.[49–51]

In order to reveal the superior performance of the 3D ZnSMX electrode, the cyclic voltammetry tests were carried out at scan rates of 0.2 to 1.2 mV s^{-1} before and after 350 cycles at 2 A g^{-1} to gain further insight into the specific capacity recovery of the 3D ZnSMX electrode during charge/discharge processes in relation to its electrochemical kinetic behavior, as shown in Fig. 5a and d. The 3D ZnSMX electrode exhibits a similar CV curve compared to pre-cycle after 350 cycles. In addition, the electrochemical kinetics of ZnSMX are analyzed by means of the power law relationship between the measured current and the sweep rate using the equation:

$$i = av^b$$

$$\log(i) = b\log(v) + \log(a)$$

where a and b are adjustable parameters, ν is the scan rate, i is the peak current. In general, the b value close to 0.5 is indicative of diffusion-controlled behavior, whereas the b value reaches 1.0 suggesting capacitive-controlled behavior in lithium-ion storage.[52] Fig. 5b and e show the fitting results before and after 350 cycles. The b values of peak 1 and peak 2 are 0.828 and 0.838 before cycling which means both capacitance behavior and ionic diffusion behavior occur during the charging and discharging processes. However, the b values of peak 1 and peak 2 become 0.90 and 0.88 after 350 cycles. It is obvious that the b value is more biased towards 1.0 after 350 cycles, which means that it tends to be more capacitively con-

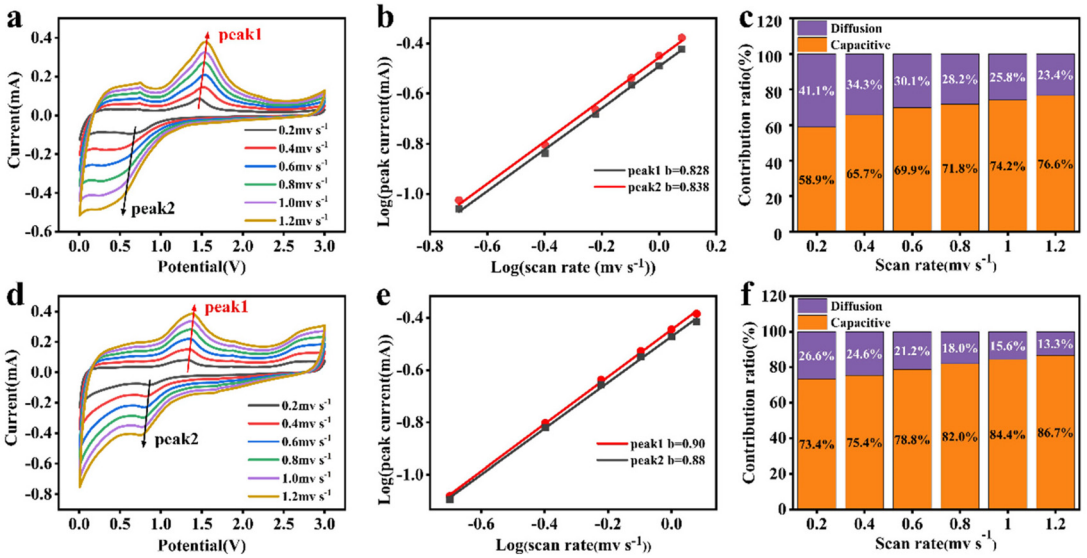

Fig. 5 (a and d) CV curves of the 3D ZnSMX electrode at different scan rates before and after 350 cycles. (b and e) *b* value in different peaks of the 3D ZnSMX electrode before and after 350 cycles. (c and f) Contribution ratios at different scan rates before and after 350 cycles.

trolled after 350 cycles. In order to gain further insight into the specific quantities of the capacitive-controlled behavior, the charge storage mechanism of the cycling process was subjected to analysis using the following equation:

$$i(v) = k_1 v + k_2 v^{1/2}$$

where k_1 and k_2 are adjustable parameters, while $k_1 v$ and $k_2 v^{1/2}$ represent the capacitive-controlled reaction current and diffusion-controlled reaction current, respectively.[53] The calculated capacitive-controlled contribution before and after 350 cycles are shown in Fig. 5c and f. It is clear that the capacitive-controlled contribution increases significantly after cycling. This increase is observed to be from 58.9% to 73.4% at 0.2 mV s^{-1} and from 76.6% to 86.7% at 1.2 mV s^{-1} after 350 cycles. Increased capacitive-controlled contribution means that well-organized interfaces in heterostructures are essential to improve fast lithium-ion storage. This predominant capacitive-controlled behavior would account for the excellent rate performance and the specific capacity recovery of 3D ZnSMX to a certain degree.[38,46]

Electrochemical impedance spectroscopy (EIS) and galvanostatic intermittent titration technique (GITT) experiments were performed to further analyze the ion transport capacity of 3D ZnSMX. As shown in Fig. 6a, the Nyquist plots are a semicircle at high and mid frequencies and a straight line at low frequencies. The semicircle represents the charge transfer impedance, while the straight line represents Li diffusion in electrodes.[39] It is evident that the MXene electrode exhibits the smallest semicircle, the 3D ZnSMX electrode is marginally larger, while the ZnS electrode is considerably the largest. This indicates that the incorporation of the MXene into ZnS nanoparticles reduces the charge transfer resistance and facilitates charge transfer kinetics. The diffusion of lithium in the 3D ZnSMX electrode is described by the Li^+ diffusion coefficient (D_{Li^+}), which is calculated according to the following formula:

$$D = \frac{4}{\pi\tau}\left(\frac{m_B V_m}{M_B S}\right)^2 \left(\frac{\Delta E_S}{\Delta E_\tau}\right)^2$$

where τ represents the relaxation time, m_B and V_m signify the mole number and mole volume of the electrode material, respectively, S denotes the electrode surface area, while ΔE_S and ΔE_τ are the transient potential changes brought about by the current pulse and the transient voltage variation in titration current flux following the relaxation period, respectively. As illustrated in Fig. 6b and c, the 3D ZnSMX exhibits a higher value of D_{Li^+} in comparison to ZnS (up to 6.3×10^{-11} cm^2 s^{-1}), thereby indicating superior electrochemical kinetics.

The SEM was employed to elucidate alterations in the surface topography of electrode sheets before and after 350 cycles. As can be observed in Fig. 6d and e, the morphology of the 3D ZnSMX electrode is almost intact after cycling, and there is no obvious crack and agglomeration during the charge and discharge process. Besides, it is more clearly observed that the overall structure of 3D ZnSMX is retained well except for a slight increase in surface roughness, which is in favor of its outstanding electrochemical performance. Nevertheless, the formation of numerous cracks is evident in the pure ZnS electrode following 350 cycles shown in Fig. 6f and g, indicating that the pure ZnS electrode is unable to maintain stability throughout the cycling process. The formation of cracks on the electrode sheets may be attributed to the structural collapse of ZnS, which is caused by significant volume changes that occur during the charging and discharging processes. Fig. S10† shows the XPS spectra of the electrode sheet after 350 cycles at a current density of 2 A g^{-1}. The binding energies of O 1s at 529.5 eV, 530.3 eV, 531.3 eV, and 533.2 eV are identi-

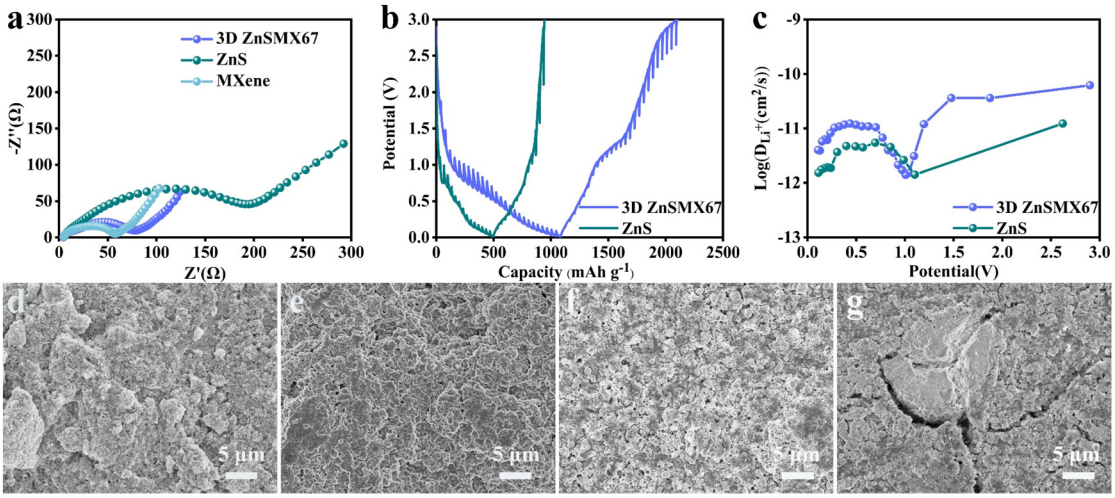

Fig. 6 (a) EIS diagram of the 3D ZnSMX, ZnS and MXene electrodes. (b and c) GITT profiles with the calculated Li^+ diffusion coefficient (D_{Li^+}). (d and e) SEM images of 3D ZnSMX electrode before and after 350 cycles. (f and g) SEM images of the ZnS electrode before and after 350 cycles.

fied as Ti–O, C–Ti–O_x, Ti–O–Zn, and O–H bonds. A comparison with Fig. 3f of the high-resolution XPS spectra of O 1s reveals that the Ti–O–Zn bond remained stable after 350 cycles.

Based on the above analysis, we can infer that the following strategically interdependent characteristics of the 3D ZnSMX electrode are responsible for the outstanding LIB performance. Firstly, the composite of MXene and ZnS nanoparticles enhances electrical conductivity, providing efficient channels for rapid electron/ion transport and improving the utilization of active materials. Secondly, the ZnS nanoparticles are tightly anchored to the MXene nanosheets through Ti–O–Zn bonds, preventing aggregation and volume expansion/shrinkage, thus ensuring excellent long-term cycling stability. Moreover, the 3D porous structure inhibits the self-stacking of MXene nanosheets and provides additional space to sustain swelling, favoring the stability of the structure and exposing more active sites. Finally, the surface-dominated lithium storage behavior of 3D ZnSMX is highly reversible, and rapid lithium diffusion enhances the cycling and rate performance of the material. Therefore, the prepared 3D ZnSMX can address the issues of poor conductivity and volume change of the ZnS anode in two ways, which is helpful in guiding the design of other TMS electrodes.

4. Conclusions

In summary, ZnS nanoparticles were grown *in situ* on MXene nanosheets and assembled into a 3D structure to form 3D ZnSMX using the *in situ* growth and template methodology. The formation of Ti–O–Zn bonds allows ZnS nanoparticles to be firmly attached to MXene nanosheets, effectively preventing the detachment of ZnS nanoparticles from the conducting MXene substrate and adapting to the volume changes of ZnS during the charge/discharge process. Moreover, the introduction of the MXene effectively enhanced the electrical conductivity of the heterostructures thereby accelerating the electron transport while simultaneously preventing the aggregation of ZnS nanoparticles. Besides, the 3D porous structure prevents the self-stacking of MXene nanosheets, thereby exposing a larger number of reactive sites and speeding up the electrochemical kinetics. The 3D ZnSMX exhibits a high capacity (782.1 mA h g^{-1} at 1 A g^{-1}), superior cycling stability (1027.8 mA h g^{-1} after 350 cycles at 2 A g^{-1}), and excellent rate performance (598.1 mA h g^{-1} at 5 A g^{-1}), which are ascribed to the capacitive-controlled lithium storage behavior with excellent electrochemical kinetics. Therefore, anchoring nano-sized ZnS on MXene nanosheets with strong interfacial interactions and preparing them into three-dimensional structures is a promising strategy for improving the lithium storage performance, which can also be extended to other metal sulfides for energy storage applications.

Data availability

The data that support the findings of this study are available in the ESI† of this article.

Conflicts of interest

There are no conflicts of interest to declare.

Acknowledgements

This work was supported by the National Natural Science Foundation of China (Grant No. 52372281), the Fundamental Research Funds for the Central Universities (2232024G-07), the State Key Laboratory for Modification of Chemical Fibers and Polymer Materials (KF2517), and the the Program for Professor of Special Appointment (Eastern Scholar) at Shanghai Institutions of Higher Learning.

References

1 M. Armand and J. M. Tarascon, *Nature*, 2008, **451**, 652–657.
2 J. M. Tarascon and M. Armand, *Nature*, 2001, **414**, 359–367.
3 J. Ma, H. Zhang, R. Liu, W. Zhang, S. Han, J. Han, G. Xu, L. Li, Y. S. He and Z. F. Ma, *Sci. China Mater.*, 2023, **66**, 493–504.
4 W. Q. Du, Y. Q. Zheng, X. Y. Liu, J. Cheng, A. Zeb, X. M. Lin, Y. F. Luo and R. C. K. Reddy, *Chem. Eng. J.*, 2023, **451**, 138626.
5 C. Lamiel, I. Hussain, H. Rabiee, O. R. Ogunsakin and K. Zhang, *Coord. Chem. Rev.*, 2023, **480**, 215030.
6 R. M. Bhattarai, N. Le, K. Chhetri, D. Acharya, S. M. S. Pandiyarajan, S. Saud, S. J. Kim and Y. S. Mok, *Adv. Sci.*, 2024, **11**, 2308160.
7 H. Yin, L. Jia, H. Y. Li, A. Liu, G. Y. Liu, Y.-C. Zhu, J. L. Huang, M. L. Cao and Z. H. Hou, *J. Energy Storage*, 2023, **65**, 107354.
8 S. Yao and Y. Sun, *J. Mater. Chem. A*, 2024, **12**, 17213–17221.
9 C. H. Lai, M. Y. Lu and L. J. Cheng, *J. Mater. Chem.*, 2012, **22**, 19–30.
10 H. Zhang, D. F. Yu, F. Z. Yuan, Y. C. Jin, L. Song, M. D. Zhang and H. G. Zheng, *Chem. Eng. J.*, 2024, **489**, 151318.
11 S. Chen, G. J. Li, M. C. Yang, J. B. Xiong, S. Akter, L. W. Mi and Y. Q. Li, *Appl. Surf. Sci.*, 2021, **535**, 147748.
12 Y. Zhao, Z. L. Zhang, X. Y. Ling, X. J. Xu, L. F. Ma and H. Pang, *J. Energy Storage*, 2021, **39**, 102611.
13 L. F. Zhai, J. M. Yu, T. Yang, H. Li, Z. Pan and W. W. Xiong, *Chem. Eng. J.*, 2023, **477**, 147114.
14 T. Y. Hou, B. R. Liu, X. H. Sun, A. R. Fun, Z. K. Xu, S. Cai, C. Z. Zheng, G. H. Yu and A. Tricoli, *ACS Nano*, 2021, **15**, 6735–6746.
15 M. Naguib, O. Mashtalir, J. Carle, V. Presser, J. Lu, L. Hultman, Y. Gogotsi and M. W. Barsoum, *ACS Nano*, 2012, **6**, 1322–1331.
16 M. R. Lukatskaya, O. Mashtalir, C. E. Ren, Y. D. Agnese, P. Rozier, P. L. Taberna, M. Naguib, P. Simon, M. W. Barsoum and Y. Gogotsi, *Science*, 2013, **34**, 1502–1505.
17 Z. G. Zou, Q. Wang, J. Yan, K. Zhu, K. Y. G. Wang and D. X. Cao, *ACS Nano*, 2021, **15**, 12140–12150.
18 S. C. Wei, Y. Fu, P. Roy, X. Tong, H. Y. Yue, M. M. Liu, H. N. Jaiswal, S. Shahi, Y. I. Gata, T. Butler, H. M. Li, Q. X. Jia and F. Yao, *ACS Appl. Mater. Interfaces*, 2022, **14**, 35673–35681.
19 C. Zhao, Z. Y. Wei, J. Zhang, P. He, X. X. Huang, X. M. Duan, D. C. Jia and Y. Zhou, *J. Alloys Compd.*, 2022, **907**, 164428.
20 X. Q. Chang, Q. Z. Zhu, Q. Zhao, P. Zhang, N. Sun, R. A. Soomro, X. X. Wang and B. Xu, *ACS Appl. Mater. Interfaces*, 2023, **15**, 7999–8009.
21 Z. H. Zhang, H. J. Ying, P. F. Huang, S. L. Zhang, Z. Zhang, T. T. Yang and W. Q. Han, *Chem. Eng. J.*, 2023, **451**, 138785.
22 G. Wang, C. F. Li, D. Estevez, P. Xu, M. Y. Peng, H. J. Wei and F. X. Qin, *Nano-Micro Lett.*, 2023, **15**, 152.
23 C. E. Ren, M. Q. Zhao, T. Makaryan, J. Halim, M. Boota, S. Kota, B. Anasori, M. W. Barsoum and Y. Gogotsi, *ChemElectroChem*, 2016, **3**, 689–693.
24 P. Zhang, R. A. Soomro, Z. X. Guan, N. Sun and B. Xu, *Energy Storage Mater.*, 2020, **29**, 163–171.
25 Z. L. Wang, J. R. Bai, H. Y. Xu, G. Chen, S. F. Kang and X. Li, *J. Colloid Interface Sci.*, 2020, **577**, 329–336.
26 L. Yao, Q. F. Gu and X. B. Yu, *ACS Nano*, 2021, **15**, 3228–3240.
27 M. Ghidiu, M. R. Lukatskaya, M. Q. Zhao, Y. Gogotsi and M. W. Barsoum, *Nature*, 2014, **516**, 78–81.
28 X. Q. Xie, M. Q. Zhao, B. Anasori, K. Maleski, C. E. Ren, J. W. Li and B. W. Byles, *Nano Energy*, 2016, **26**, 513–523.
29 B. M. Jun, C. M. Park, J. Heo and Y. Yoon, *J. Environ. Manage.*, 2020, **256**, 109940.
30 M. Shekhirev, C. E. Shuck, A. Sarycheva and Y. Gogotsi, *Prog. Mater. Sci.*, 2021, **120**, 100757.
31 Q. Chen, Y. Wei, X. K. Zhang, Z. L. Yang, F. Wang, W. Liu, J. H. Zuo, X. K. Gu, Y. Yao, X. G. Wang, F. Zhao, S. B. Yang and Y. J. Gong, *Adv. Energy Mater.*, 2022, **12**, 2200072.
32 C. L. Wei, B. J. Xi, P. Wang, Y. Z. Liang, Z. R. Wang, K. D. Tian, J. K. Feng and S. L. Xiong, *Adv. Mater.*, 2023, **35**, 2303780.
33 H. Wang, K. Xie, Y. You, Q. Hou, K. Zhang, N. Li, W. Yu, K. P. Loh, C. Shen and B.-Q. Wei, *Adv. Energy Mater.*, 2019, **9**, 1901806.
34 H. Liu, Z. J. Xu, B. Cao, Z. J. Xin, H. J. Lai, S. Gao, B. Xu, J. L. Yang, T. Xiao, B. Zhang and H. J. Fan, *Adv. Energy Mater.*, 2024, **14**, 2400318.
35 B. Cao, H. Liu, X. Zhang, P. Zhang, Q. Z. Zhu, H. L. Du, L. L. Wang, R. P. Zhang and B. Xu, *Nano-Micro Lett.*, 2021, **13**, 202.
36 Y. Zhao, Z. L. Zhang, X. Y. Ling, X. J. Xu, L. F. Ma and H. Pang, *J. Energy Storage*, 2021, **39**, 102611.
37 S. Lee, S. Kim, J. Gim, M. H. Alfaruqi, S. Kim, V. Mathew, B. Sambandam, J. Hwang and J. Kim, *Composites, Part B*, 2022, **231**, 109548.
38 W. L. Zhang, Z. Y. Huang, H. H. Zhou, S. L. Li, C. Q. Wang, H. X. Li, Z. H. Yan, F. Wang and Y.-F. Kuang, *J. Alloys Compd.*, 2020, **816**, 152633.
39 C. Z. Ke, R. W. Shao, Y. G. Zhang, Z. F. Sun, S. Qi, H. H. Zhang, M. Li, Z. L. Chen, Y. S. Wang, B. S. Sa, H. C. Lin, H. D. Liu, M. S. Wang, S. Q. Chen and Q. B. Zhang, *Adv. Funct. Mater.*, 2022, **32**, 2205635.
40 W. X. Zhang, L. Y. Yang and S. Yin, *J. Colloid Interface Sci.*, 2024, **667**, 741–750.
41 Q. Q. Liang, L. X. Zhang, M. Zhang, Q. C. Pan, L. C. Wang, G. H. Yang, F. H. Zheng, Y. G. Huang, H. Q. Wang and Q. Y. Li, *Chem. Phys. Lett.*, 2021, **775**, 138662.
42 L. X. Zhang, M. Zhang, F. Peng, Q. C. Pan, H. Q. Wang, F. H. Zheng, Y. G. Huang and Q. Y. Li, *J. Alloys Compd.*, 2022, **910**, 164908.
43 Y. Y. Han, X. F. Zhang, B. C. Chen, P. W. Huang, Y. Chai, X. H. Wu and Z. L. Xie, *Dalton Trans.*, 2023, **52**, 16336–16344.
44 X. J. Xu, F. K. Li, D. C. Zhang, Z. B. Liu, S. Y. Zuo, Z. Y. Zeng and J. Liu, *Adv. Sci.*, 2022, **9**, 2200247.

45 Y. Rao, K. J. Zhu, H. C. Li, P. H. Liang, H. J. Zheng, J. Y. Chen, J. Zhang, J. S. Liu, K. Yan and J. Wang, *Electrochim. Acta*, 2022, **436**, 141264.
46 Y. S. Choi, W. Choi, W. Yoon and J. M. Kim, *ACS Nano*, 2022, **16**, 631–642.
47 Y. Zhang, P. X. Wang, Y. Y. Yin, X. Y. Zhang, L. S. Fan, N. Q. Zhang and K. N. Sun, *Chem. Eng. J.*, 2019, **356**, 1042–1051.
48 B. C. Chen, X. Lu, H. Y. Zhong, P. W. Huang, Y. N. Wu, S. Y. Yu, K. Z. Du and X. H. Wu, *J. Mater. Chem. A*, 2022, **10**, 25671–25682.
49 Z. Y. Wang, D. Y. Luan, S. Madhavi, Y. Hu and X. W. D. Lou, *Energy Environ. Sci.*, 2012, **5**, 5252–5256.
50 C. Z. Ke, R. W. Shao, Y. G. Zhang, Z. F. Sun, S. Qi, H. H. Zhang, M. Li, Z. L. Chen, Y. S. Wang, B. Sa, H. C. Lin, H. D. Liu, M. S. Wang, S. Q. Chen and Q. B. Zhang, *Adv. Funct. Mater.*, 2022, **32**, 2205635.
51 Y. F. Dong, M. L. Yu, Z. Y. Wang, Y. Liu, X. Z. Wang, Z. B. Zhao and J. S. Qiu, *Adv. Funct. Mater.*, 2016, **26**, 7590–7598.
52 W. X. Zhang, C. Hu, J. M. Zhang, X. J. Zhao, S. L. Lu, L. Yang and S. G. Yin, *J. Energy Storage*, 2024, **76**, 109596.
53 K. Y. Feng, Y. X. Li, C. Y. Xu, M. Zhang, X. Yang, Y. Cheng, Y. L. Wang, L. Y. Yang and S. G. Yin, *Electrochim. Acta*, 2023, **444**, 142022.